ACSNANO

www.acsnano.org

ARTICLE

# Efficient Polymer-Mediated Delivery of Gene-Editing Ribonucleoprotein Payloads through Combinatorial Design, Parallelized Experimentation, and Machine Learning

Ramya Kumar, Ngoc Le, Zhe Tan, Mary E. Brown, Shan Jiang, and Theresa M. Reineke*

Cite This: *ACS Nano* 2020, 14, 17626–17639

Read Online

ACCESS | Metrics & More | Article Recommendations | Supporting Information

**ABSTRACT:** Chemically defined vectors such as cationic polymers are versatile alternatives to engineered viruses for the delivery of genome-editing payloads. However, their clinical translation hinges on rapidly exploring vast chemical design spaces and deriving structure–function relationships governing delivery performance. Here, we discovered a polymer for efficient intracellular ribonucleoprotein (RNP) delivery through combinatorial polymer design and parallelized experimental workflows. A chemically diverse library of 43 statistical copolymers was synthesized *via* combinatorial RAFT polymerization, realizing systematic variations in physicochemical properties. We selected cationic monomers that varied in their p$K_a$ values (8.1–9.2), steric bulk, and lipophilicity of their alkyl substituents. Co-monomers of varying hydrophilicity were also incorporated, enabling elucidation of the roles of protonation equilibria and hydrophobic–hydrophilic balance in vehicular properties and performance. We screened our multiparametric vector library through image cytometry and rapidly uncovered a hit polymer (P38), which outperforms state-of-the-art commercial transfection reagents, achieving nearly 60% editing efficiency *via* nonhomologous end-joining. Structure–function correlations underlying editing efficiency, cellular toxicity, and RNP uptake were probed through machine learning approaches to uncover the physicochemical basis of P38's performance. Although cellular toxicity and RNP uptake were solely determined by polyplex size distribution and protonation degree, respectively, these two polyplex design parameters were found to be inconsequential for enhancing editing efficiency. Instead, polymer hydrophobicity and the Hill coefficient, a parameter describing cooperativity-enhanced polymer deprotonation, were identified as the critical determinants of editing efficiency. Combinatorial synthesis and high-throughput characterization methodologies coupled with data science approaches enabled the rapid discovery of a polymeric vehicle that would have otherwise remained inaccessible to chemical intuition. The statistically derived design rules elucidated herein will guide the synthesis and optimization of future polymer libraries tailored for therapeutic applications of RNP-based genome editing.

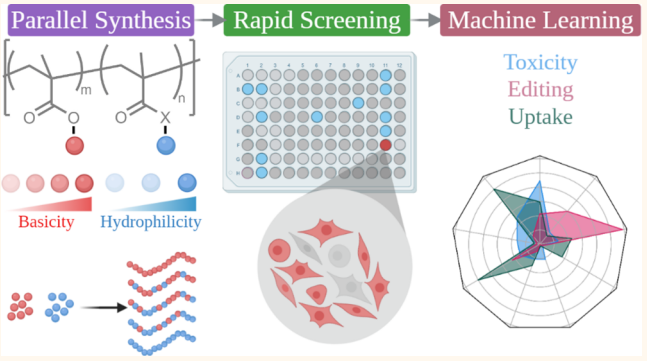


**KEYWORDS:** *polymeric gene delivery, CRISPR, ribonucleoproteins, high-throughput experimentation, machine learning*

Genome-editing platforms based on clustered regularly interspersed palindromic repeats (CRISPR) have transformed the therapeutic landscape for diseases where healthy cellular states can be restored through the deletion, insertion, or repair of genetic sequences.[1,2] Recent clinical trials of investigational gene therapeutics for β-thalassemia and sickle cell disease suggest that the CRISPR gene-editing platform is safe and efficacious.[3,4] Additional clinical trials are underway to develop CRISPR-focused therapeutics for debilitating conditions such as Duchenne's muscular dystrophy, Leber congenital amaurosis, and chimeric antigen receptor T-cell therapies for cancer.[5,6] Despite the immense curative potential of CRISPR, widespread clinical deployment faces an uncertain outlook due to excessive

Received: October 13, 2020
Accepted: November 17, 2020
Published: November 23, 2020






https://dx.doi.org/10.1021/acsnano.0c08549
*ACS Nano* 2020, 14, 17626–17639

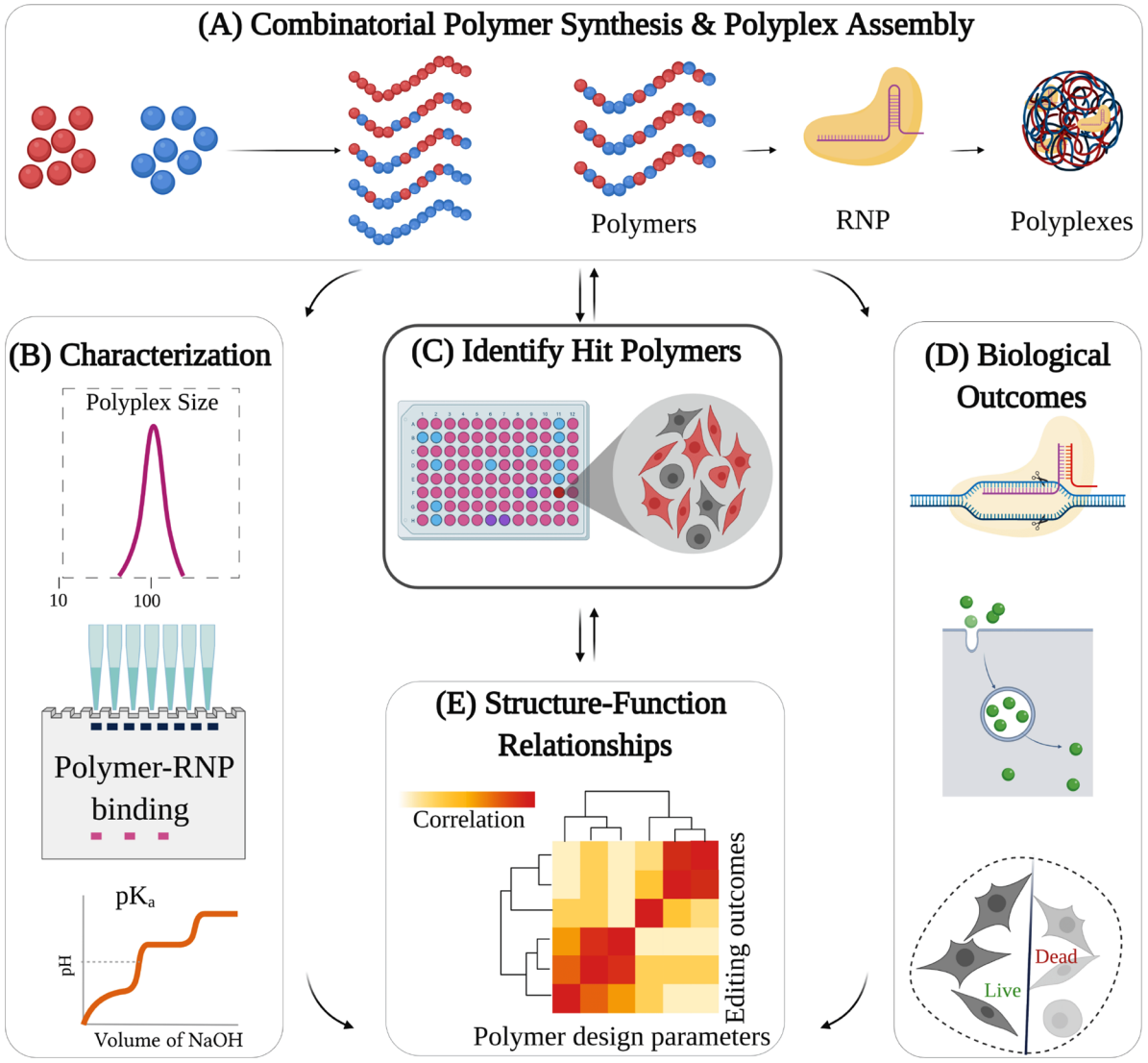


**Figure 1. Overview of workflow used in this contribution. (A) Following combinatorial RAFT polymerization using a parallel synthesizer, polymers were assembled with RNP payloads. (C) Gene-editing efficiency was evaluated through high-throughput biological assays. (B) Polymers were characterized in parallel to probe protonation behavior, RNP binding affinity, polyplex size distribution, and charge density. (D) Library-wide measurements of polyplex internalization and toxicity were completed in parallel. (E) Finally, machine learning tools were deployed to mine experimental data sets and generate structure−function maps correlating polymer attributes with RNP delivery, cellular toxicity, and RNP uptake.**

reliance on engineered viral vectors.[7,8] Production of clinical grade viruses involves prohibitive costs and logistical bottlenecks, while the scale-up of viral vectors for large patient populations has to contend with regulatory issues. In addition to manufacturing and regulatory delays caused by viral vectors, they are limited in their cargo capacity, and this size ceiling is particularly problematic in the context of bulky cargoes.[9] For example, adeno-associated viruses, a widely used therapeutic vehicle that is considered to be among the safest viral vectors, can only accommodate 4.5 kbp, limiting its adoption for multicomponent CRISPR cargoes.[10] Although advances in viral vector engineering have minimized occurrences of carcinogenic mutations, genomic integration, and fatal systemic inflammatory responses, these risks are amplified when repeated dosing or large dosages are involved.[11] In order to engineer safe, scalable, and affordable CRISPR therapeutics, we must meet the urgent need for replacing viral gene carriers with synthetic materials.[12]

Developing biomaterials to deliver gene therapeutics is a design challenge spanning several length scales, temporal horizons, and biological barriers within a delicate delivery cascade.[13] As a first step, polymeric vehicles are expected to condense the CRISPR payloads (mRNA, plasmids, or ribonucleoproteins) into discrete nanosized polyelectrolyte complexes termed polyplexes. Polyplexes must subsequently navigate extracellular barriers such as serum DNAases (or RNAases) and reticuloendothelial system clearance, as well as intracellular barriers such as endosomal interrogation and lysosomal degradation.[14] Finally the cargo must be released within a narrow spatiotemporal window that is optimal for payload translocation to the nucleus, where they can undergo further processing and realize targeted edits.[15] In addition to fulfilling exacting specifications for safety, efficiency, and cost-effectiveness, synthetic vectors must minimize immune activation and cellular toxicity.[16] Since nonviral gene delivery imposes stringent design specifications and demands precise


https://dx.doi.org/10.1021/acsnano.0c08549
ACS Nano 2020, 14, 17626−17639

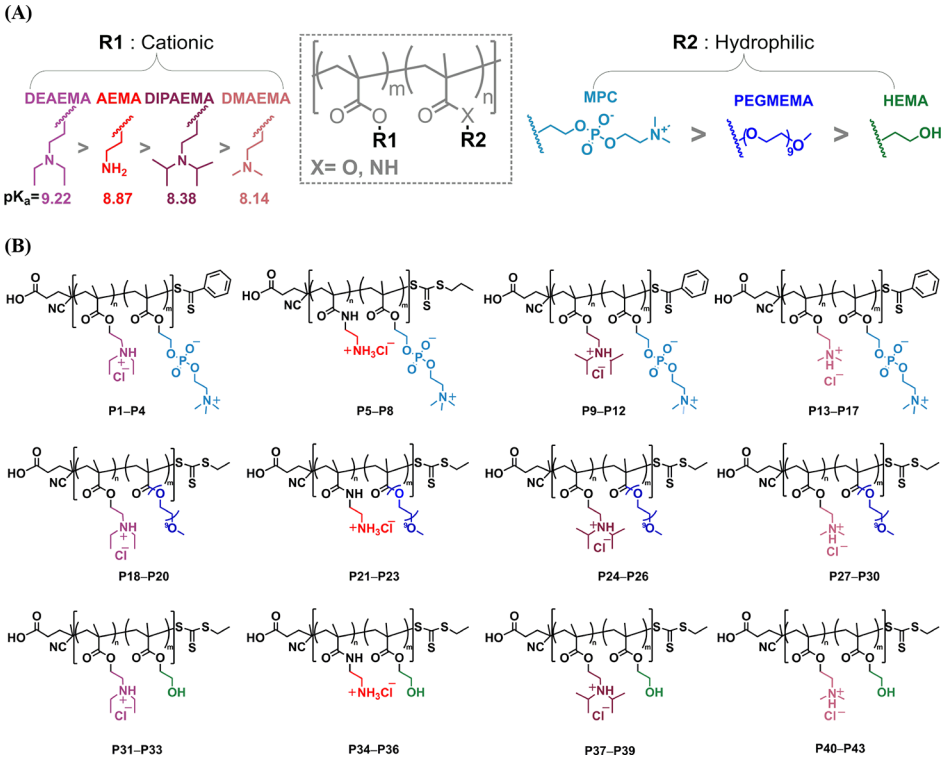


**Figure 2. Scheme for combinatorial RAFT polymerization. Cationic monomers ($pK_a$ values between 8.14 and 9.22) were copolymerized with neutral monomers of varying hydrophilicity. The targeted cationic monomer incorporation was varied systematically from 0% to 100% in 25% increments, ultimately giving rise to 43 statistical copolymers of systematically varied interfacial properties.**

control over interfacial properties, polymer chemistry is well-suited to generate vehicles for nucleic acid cargoes. Advances in controlled radical polymerization methods such as reversible addition fragmentation transfer polymerization (RAFT) have enabled access to diverse polymer architectures. A continually expanding monomer scope and progress in fine-tuning polymerization kinetics have ensured that we can synthesize polymers of any desired chemical composition, architecture, and molecular weight distributions, allowing us to create multifunctional gene delivery vehicles with exquisitely tailored properties.[17] Unlike engineered viruses, the mass manufacture of polymers does not present logistical and economic challenges.

By incorporating monomers in different ratios, architectures, and lengths, we can generate almost infinite structurally distinct design possibilities. Although polymer chemists can produce portfolios of macromolecules on demand, it is difficult to predict from first-principles whether the synthesized polymers will satisfy design requirements for a given therapeutic application. Since the biological milieu in which payloads are delivered by polymeric vectors is complex, *ab initio* prediction of gene-editing efficiency directly from polymer structure is almost impossible. For example, the proton-sponge hypothesis[18] has confounded efforts to acquire a nuanced physical understanding of the precise role played by polycations in intracellular trafficking of their payloads.[19] Similarly, studies exploring the role of design facets such as polymer hydrophobicity,[20−22] PEGylation,[23] protein corona formation,[24] and polyplex diameter[25] during transfection have seldom converged on a single answer. With neither theoretical models nor heuristic knowledge providing reliable experimental guidance, it is challenging to explore the polymer design space in a manner that minimizes experimental effort and accelerates polymer discovery. Recognizing the urgent clinical need for nonviral vectors, we deployed parallelized experimentation and machine learning to rapidly discover high-performing polymeric vehicles for ribonucleoproteins (RNPs). We draw attention to previous studies where combinatorial libraries of cationic lipids,[26−31] polymers,[23,32−40] and gold nanoparticles[41−43] were screened to identify high-performing synthetic gene delivery vectors rapidly. Although the application of high-throughput approaches is becoming more widespread in gene delivery,[44] the elucidation of structure−function relationships from large data sets and the development of predictive models that identify correlations between biological responses and polymer attributes has received scant attention. In contrast to previous studies that focused mainly on exploiting serendipity to discover high-performing materials, our study goes beyond hit identification by answering the following questions: (1) Which interfacial properties favor efficient intracellular delivery of RNPs? (2) How do we design polymers that realize these optimal properties?

To facilitate rapid clinical translation of polymeric vehicles, we must explore multidimensional chemical design spaces efficiently. Hence, we integrated combinatorial polymer design, parallel synthesis, image cytometry, high-throughput biological assays, and machine learning into a streamlined polymer discovery workflow (Figure 1) that (1) speedily discovers "hit polymers" from unexpected regions in chemical space, (2) identifies design rules latent within serendipitously discovered polymers, and (3) generates overarching structure−function correlations that can be broadly applied to design future polymer libraries. Through image cytometric screening, we identified a lead structure (P38), which outperformed four state-of-the-art commercial transfection reagents. Sanger sequencing confirmed that P38 achieved 58% indel formation,


https://dx.doi.org/10.1021/acsnano.0c08549
ACS Nano 2020, 14, 17626−17639

**Table 1. Characterization *via* NMR, SEC, Titration, and Electrophoresis**

| | | | | | NMR | SEC | | titration | electrophoresis |
|---|---|---|---|---|---|---|---|---|---|
| entry | polymer | $m$ | $n$ | % cat. (target) | % cat. | $M_w$ (kDa) | $Đ$ | p$K_a$ | $\zeta$ (mV) |
| P1 | p(DEAEMA$_m$-*st*-MPC$_n$) | 98 | | 100 | 100 | 19.4 | 1.05 | 6.7 | 12.4 |
| P2 | | 43 | 38 | 75 | 53 | 20.3 | 1.03 | | −14.1 |
| P3 | | 42 | 58 | 50 | 42 | 26.9 | 1.06 | | −0.05 |
| P4 | | 43 | 81 | 25 | 35 | 34.5 | 1.08 | | −5.18 |
| P5 | p(AEMA$_m$-*st*-MPC$_n$) | 67 | | 100 | 100 | 14.3 | 1.26 | 8.1 | 15.2 |
| P6 | | 50 | 23 | 75 | 68 | 19 | 1.24 | 8 | 12.8 |
| P7 | | 43 | 51 | 50 | 46 | 25 | 1.12 | 7.9 | 2.9 |
| P8 | | 19 | 61 | 25 | 24 | 22.8 | 1.05 | 6.8 | 6.9 |
| P9 | p(DIPAEMA$_m$-*st*-MPC$_n$) | 80 | | 100 | 100 | 18.2 | 1.05 | 5.9 | 20.8 |
| P10 | | 76 | 36 | 75 | 68 | 28.2 | 1.04 | 6.4 | 5.6 |
| P11 | | 73 | 58 | 50 | 56 | 35.4 | 1.08 | 6.9 | 2.2 |
| P12 | | 34 | 83 | 25 | 29 | 32.8 | 1.03 | | −13.8 |
| P13 | p(DMAEMA$_m$-*st*-MPC$_n$) | 110 | | 100 | 100 | 18.4 | 1.04 | 6.9 | 21.7 |
| P14 | | 24 | 9 | 75 | 72 | 7.2 | 1.07 | 6.9 | 5.6 |
| P15 | | 47 | 33 | 50 | 59 | 17.6 | 1.02 | 7.5 | 3.8 |
| P16 | | 17 | 47 | 25 | 26 | 17.4 | 1.03 | 7.8 | 0 |
| P17 | | | 24 | 0 | 0 | 11.3 | 1.12 | | −10.9 |
| P18 | p(DEAEMA$_m$-*st*-PEGMEMA$_n$) | 70 | 21 | 75 | 77 | 25.6 | 1.08 | 6.9 | 4.2 |
| P19 | | 47 | 44 | 50 | 52 | 33.6 | 1.09 | 6.6 | −7.1 |
| P20 | | 33 | 66 | 25 | 33 | 43.9 | 1.16 | 6.5 | −11.7 |
| P21 | p(AEMA$_m$-*st*-PEGMEMA$_n$) | 85 | 35 | 75 | 71 | 38.5 | 1.21 | 7.8 | 16.2 |
| P22 | | 90 | 120 | 50 | 43 | 92.8 | 1.23 | 8.1 | 8.6 |
| *P*23 | | 44 | 79 | 25 | 36 | 55.9 | 1.19 | 7.8 | 7 |
| P24 | p(DIPAEMA$_m$-*st*-PEGMEMA$_n$) | 36 | 20 | 75 | 64 | 18.4 | 1.04 | 6.6 | 6.3 |
| P25 | | 29 | 33 | 50 | 47 | 24.4 | 1.06 | 6.8 | 2.3 |
| P26 | | 25 | 76 | 25 | 25 | 48.5 | 1.11 | 6.9 | −9.4 |
| P27 | p(DMAEMA$_m$-*st*-PEGMEMA$_n$) | 26 | 9 | 75 | 74 | 10.4 | 1.18 | 7 | 8.3 |
| P28 | | 13 | 12 | 50 | 52 | 10.6 | 1.23 | 7 | 18.5 |
| P29 | | 1 | 6 | 25 | 12 | 3.8 | 1.09 | 6.8 | −0.09 |
| P30 | | | 7 | 0 | 0 | 6.4 | 1.77 | | 6.8 |
| P31 | p(DEAEMA$_m$-*st*-HEMA$_n$) | 60 | 21 | 75 | 74 | 14.7 | 1.04 | 7.5 | 15.2 |
| P32 | | 47 | 47 | 50 | 50 | 16.1 | 1.07 | 7.6 | 9.4 |
| P33 | | 22 | 51 | 25 | 30 | 11.6 | 1.06 | 7.8 | 5.6 |
| P34 | p(AEMA$_m$-*st*-HEMA$_n$) | 85 | 54 | 75 | 61 | 26.2 | 1.23 | 8.2 | 22.7 |
| P35 | | 72 | 92 | 50 | 44 | 29.6 | 1.23 | 8.2 | 21 |
| P36 | | 40 | 132 | 25 | 23 | 27.1 | 1.13 | 6.9 | 18.4 |
| P37 | p(DIPAEMA$_m$-*st*-HEMA$_n$) | 62 | 33 | 75 | 65 | 19 | 1.07 | 6.5 | 16.2 |
| P38 | | 52 | 50 | 50 | 51 | 20.2 | 1.13 | 7.3 | 12.8 |
| P39 | | 27 | 80 | 25 | 25 | 17.4 | 1.07 | 6.4 | −0.7 |
| P40 | p(DMAEMA$_m$-*st*-HEMA$_n$) | 34 | 22 | 75 | 60 | 8.8 | 1.04 | 7.2 | 4.8 |
| P41 | | 32 | 45 | 50 | 42 | 11.7 | 1.05 | 7.2 | 7.9 |
| P42 | | 65 | 145 | 25 | 31 | 31.6 | 1.09 | 7.3 | 2.5 |
| P43 | | | 60 | 0 | 0 | 8.6 | 1.04 | | 0.8 |

an editing efficiency that is 2-fold higher than Lipofectamine CRISPRMAX and JetCRISPR. Having established the superlative editing performance of P38, we employed machine learning to identify structural drivers associated with cellular toxicity, editing efficiency, and cellular internalization of RNP payloads. While polycation protonation favored polymer-mediated RNP uptake, it did not contribute to efficient intracellular delivery of RNPs. Instead, we must engineer hydrophobic polymers that possess high Hill coefficients and deprotonate with a high degree of cooperativity, allowing for rapid unpackaging of RNP payloads within the cytosol. We posit that efficient intracellular RNP delivery performance can be achieved by implementing the following polymer design rules: (1) selecting moderately hydrophilic co-monomers while avoiding superhydrophilic motifs and (2) incorporating steric bulk and lipophilicity[20,45] within tertiary amine methacrylates to promote hydrophobic collapse and cooperative polymer deprotonation. Our powerful discovery pipeline can be applied across diverse cell types and biological cargoes to individually tailor the properties of polymeric vehicles for varied clinical goals, transforming the therapeutic landscape for genome editing.

## RESULTS AND DISCUSSION

**Parallel Synthesis and Characterization of a Combinatorially Designed Polymer Library.** While cationic monomers confer positive charge densities that mediate nucleic acid condensation, their reaction partners may alleviate toxicity, prolong polyplex colloidal stability, or modulate the binding equilibrium of the polyplexes. Pairing three hydro-


https://dx.doi.org/10.1021/acsnano.0c08549
ACS Nano 2020, 14, 17626−17639

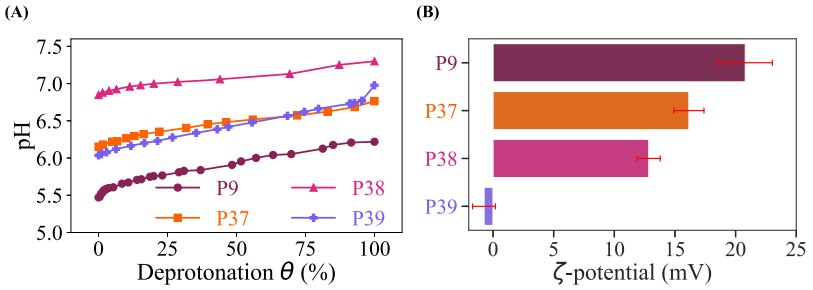


**Figure 3. Effect of co-monomer incorporation on polycation protonation is illustrated through the example of the p(DIPAEMA-*st*-HEMA) series of polymers (P9, P37−P39). (A) The p$K_a$ values of four polycations in this polymer subfamily were determined through potentiometric titrations. Changes in pH have been plotted as a function of the degree of deprotonation, $\theta$. (B) Electrophoretic mobilities of polymers were measured in PBS to monitor changes in $\zeta$-potential with decreasing cationic monomer incorporation.**

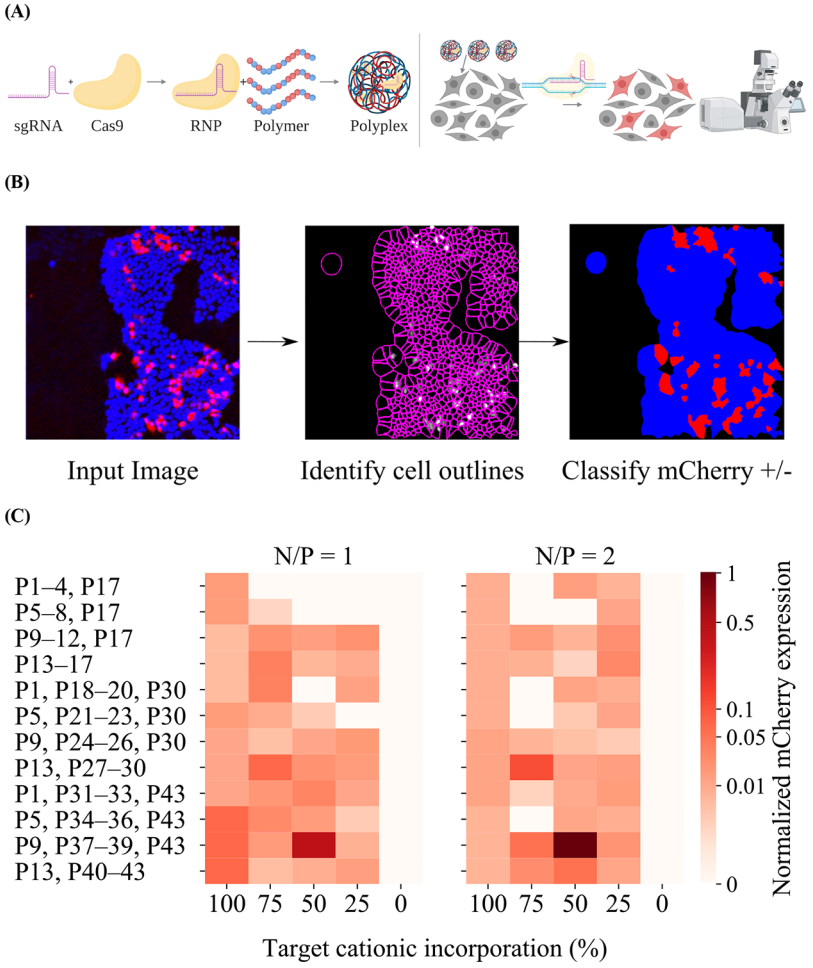


**Figure 4. (A) Overview of screening workflow. In the HEK293 TLR cell line, if 100% editing efficiency were achieved *via* NHEJ, about one-third of cells would produce mCherry, allowing us to adopt mCherry expression levels as an indirect measure of editing efficiency. To quantify mCherry expression and gene-editing outcomes with high throughput, while ensuring adequate sensitivity to low gene-editing efficiencies, image cytometry was employed in tandem with (B) high-content image analysis software pipelines. (C) RNP delivery was assessed at two N/P ratios (1 and 2) across the entire library. At the end of the screening study, P38 ($p$(DIPAEMA$_{52}$-*st*-HEMA$_{50}$)) emerged as the primary hit polymer.**

philic monomers with four cationic monomers gives rise to 12 binary copolymers. Within each binary copolymer, we varied the polymer composition to target cationic monomer incorporations of 100%, 75%, 50%, 25%, and 0% (Figure 2). Overall, a library of 43 well-defined copolymers was generated using RAFT polymerization (Table 1). Subsequent to synthesis, we measured (1) polymer composition (0−100% cationic monomer incorporation), (2) molecular weight distribution (9−49 kDa), (3) $\zeta$-potential (−15 to +23 mV), and (4) p$K_a$ (5.9−9) of all polymers within the library. Systematic variations to polymer composition were introduced through combinatorial design, resulting in polyplex hydrodynamic radii ranging from 6 nm to nearly 2 $\mu$m (Figures S12−S14) and RNP binding affinities spanning strong, weak, and intermediate degrees of complexation (Figures S15−S17).


https://dx.doi.org/10.1021/acsnano.0c08549
ACS Nano 2020, 14, 17626−17639

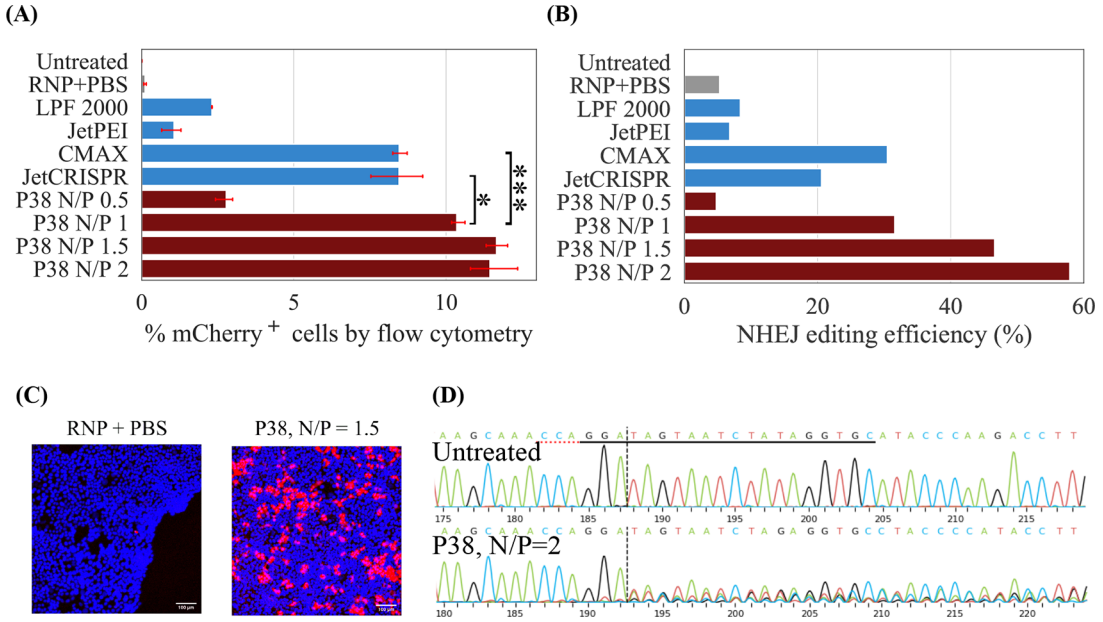


**Figure 5. (A) Flow cytometry showed that at N/P ratios of 1, 1.5, and 2, P38 resulted in higher mCherry expression than Lipofectamine CRISPRMAX (CMAX) and JetCRISPR ($n$ = 3). The mean mCherry expression of the P38 N/P 1 treatment condition was found to be significantly higher than both CMAX ($p$-value of 0.0006) and JetCRISPR ($p$-value of 0.0213). (B) NHEJ editing measured by Sanger sequencing and TIDE assay. Sanger sequencing established that P38 outperforms commercial controls, achieving 58% editing efficiency. (C) mCherry expression in cells treated with unpackaged ribonucleoprotein and polyplexes formed with P38. Scale bar is 100 $\mu$m. (D) Representative chromatograms from cells treated with P38/RNP polyplexes at an N/P of 2.**

In most cases, the composition of polymerized products recapitulated that of the monomer feed, simplifying the realization of targeted cationic incorporation. Despite reaching high conversion (80−90%), we were able to achieve excellent control over the controlled radical polymerization kinetics ($Đ$ < 1.2) for almost the entire library while also obtaining the desired degree of polymerization (a minimum $M_n$ of 10 kDa was targeted and was attained in most instances). We also performed $\zeta$-potential measurements and p$K_a$ titrations (Table 1) to characterize surface potential and protonation equilibria, respectively. The cationic monomers vary in the type of charge center (primary *versus* tertiary amines) and encompass a range of p$K_a$ values from 8 to 9 (Figure 2); however, the p$K_a$ values of the resultant (co)polymers spanned a much broader range between 5.9 and 9 (Table 1). While cationic homopolymers typically exhibited high charge densities (as measured by the $\zeta$-potential), the installation of extremely hydrophilic functionalities such as PEG or MPC resulted in sharp declines in surface potentials.

A detailed characterization workflow was developed to comprehensively capture the most relevant physicochemical attributes of each polymer (Table 1). We highlight this workflow by showing snapshots of data collected for the p(DIPAEMA-*st*-HEMA) subfamily (P9, P37−P39) of copolymers (Figure 3), while characterization data for the remaining polymers can be found in the SI. Measurements of $\zeta$-potential revealed a generalized trend; the cationic homopolymer displayed the highest charge density, while the addition of HEMA repeat units gradually lowered the $\zeta$-potential to near-zero levels. Next, we examined the effect of copolymer composition on deprotonation by estimating p$K_a$ values *via* titration. The reduction in p$K_a$ from 8.38 to 5.9 while going from monomer to homopolymer can be attributed to the suppression of amine protonation due to electrostatic repulsion between proximate amine groups (Figures S8 and S9). In contrast, upon increasing HEMA incorporation to 25%, 50%, and 75%, p$K_a$ values increased from 5.9 for the cationic homopolymer P9 to 6.5, 7.3, and 6.4, respectively (Figure 3A). This nonmonotonic trend in p$K_a$ cannot be explained by the polymer composition alone and is a complex function of monomer distribution and polymer conformation.[46−48] Compared to the low p$K_a$ value of the cationic homopolymer (P9 had a p$K_a$ = 5.9), the copolymers incorporating HEMA exhibited p$K_a$ values that were up to 1.4 pH units higher, highlighting the critical, but frequently overlooked impact of polymer composition on polycation protonation. In summary, parallelized approaches to synthesis and characterization generated synthetic vector libraries that encompass a wide range of chemical compositions, interfacial properties, and protonation equilibria. This multiparametric polymer library helped us probe relationships between polymer properties, intracellular RNP delivery, cellular toxicity, and payload internalization, while maximizing experimental efficiency and throughput. Although larger material libraries may have been generated in previous reports, the scope of polymer characterization was severely restricted.[26,32−36] In contrast, we balanced the demands of synthetic throughput and rigorous characterization *via* parallel synthesis and high-throughput characterization workflows.

**Discovery of Hit Polymer (P38) for Functional Delivery of RNP Payloads.** To identify structures that mediate efficient genome editing, we engineered the HEK293 cell line with the traffic light reporter (TLR) gene.[49] This reporter system allows us to quantify nonhomologous end-joining (NHEJ), an imprecise and error-prone DNA-repair pathway that results in mCherry expression in this cell line.

Even if 100% NHEJ editing were to be achieved, only 33% of frameshift mutations would culminate in mCherry expression.[49] While rapid hit detection is challenging through flow cytometry, other methods are not sensitive enough to


https://dx.doi.org/10.1021/acsnano.0c08549
ACS Nano 2020, 14, 17626−17639

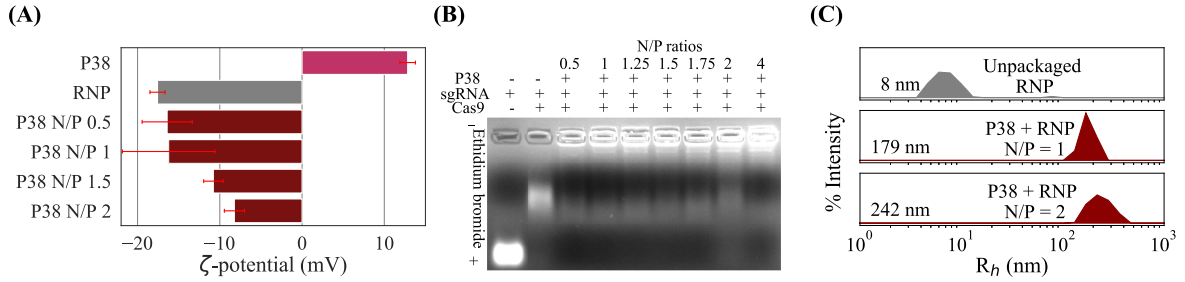


**Figure 6. (A) ζ-Potential measurements of polyplexes formulated at four N/P ratios of 0.5, 1, 1.5, and 2. (B) Gel migration assays revealed a small population of unbound RNP in the polyplexes, suggesting that the binding between P38 and RNPs is moderate. (C) Dynamic light scattering measurements ($n$ = 3−5) yielded monomodal size distributions.**

detect small populations of mCherry-expressing cells in instances of low editing efficiency. To resolve the trade-off between throughput and sensitivity, we adopted image cytometry[50] to efficiently interrogate NHEJ events mediated by polymers (Figure 4A). Using an image analysis pipeline, the spatial distribution and intensity of mCherry were quantified (Figure 4B).

To map the relationship between editing efficiencies, polymer compositions, and N/P ratio (the stoichiometric ratio of ionizable amines within the polymers to phosphate groups within guide RNA), we adopted the following procedure. First, for each polyplex formulation, mCherry expression levels were averaged across all images and normalized to the maximum value recorded in the polymer library (Figure 4C). We observed that cells treated with P38 polyplexes exhibited the highest mCherry expression levels, suggesting that this polymer achieved highly efficient intracellular RNP delivery. Excepting P38, the rest of the library resulted in either near-zero mCherry expression or marginal mCherry expression.

**P38 Outperformed Four State-of-the-Art Commercial Vehicles, 58% Editing Efficiency Achieved.** To benchmark P38 against commercially available lipid-based and polyethylenimine (PEI)-based transfection reagents, we performed flow cytometric measurements to quantify mCherry expression resulting from NHEJ editing (Figure 5A). RNP delivery by JetPEI and Lipofectamine 2000 resulted in 1% and 2% mCherry expression, respectively, suggesting that these reagents are better suited for pDNA payloads than for RNPs. The RNP-specific reagents fared better, with both Lipofectamine CRISPRMAX (CMAX) and JetCRISPR causing around 8% of cells to express mCherry. As for P38, mCherry expression was highly dependent on the dose of polymer. At an N/P ratio of 0.5, editing performance was marginal, with only 2% mCherry expression; however, N/P ratios of 1, 1.5, and 2 resulted in significant improvements over commercial controls (10−12% mCherry expression).

In the TLR cell line, mCherry expression severely underestimates the actual editing efficiency, since only a fraction of gene disruptions results in mCherry production. Therefore, it is essential to complement flow cytometry with an analysis of the distribution of insertions and deletions (indels) culminating from NHEJ (Figure 5B). Sequencing results largely mirrored the trends observed during flow cytometric measurements, establishing that mCherry expression is a valid proxy for editing efficiency. Considering only results from commercial reagent controls, we recorded the highest editing efficiency for Lipofectamine CRISPRMAX, with 30% of the cell population containing mixed DNA sequences resulting from error-prone NHEJ. JetCRISPR reported slightly lower editing frequencies than expected (20%), while less than 10% indel formation was observed for JetPEI and Lipofetcamine 2000. In contrast, P38-mediated RNP delivery led to editing efficiencies as high as 58%, which is almost double that of the most efficient among commercial transfection reagents (Lipofectamine CRISPRMAX). Taken together, flow cytometry and sequencing results offer overwhelming evidence that P38 outperforms state-of-the-art commercial vehicles.

To identify the biophysical factors associated with functional RNP delivery, we performed gel migration studies and dynamic light scattering (DLS) measurements for the entire polyplex library. Since polymeric vectors must balance payload protection and rapid intracellular unpackaging, it is essential to probe the distribution of binding states among polymer−RNP complexes using gel electrophoresis. In the case of P38, we observed that RNPs existed in two binding configurations: polymer-bound RNPs that did not migrate in response to the applied electric field and a small population of RNPs that migrated (Figure 6B) to the positive electrode. To gain further insight into polymer−RNP association, ζ-potential measurements of polyplexes were performed (Figure 6A). Since P38 has a $pK_a$ of 7.3, we expected roughly half the tertiary amines along the polymer backbone to exist in a protonated state at physiological pH, giving rise to a net positive charge (12.8 mV in PBS). The spCas9 protein is known to possess an electrostatically heterogeneous surface (Figure S27 in the SI), while the sgRNA has an anionic backbone. As a result, the RNP complex bears a charge of −17.5 mV in PBS. Among polyplex formulations with N/P ratios of 0.5 and 1, the extent of negative charge was reduced, but polarity was not reversed. Surprisingly, charge inversion was not achieved even at higher N/P ratios of 1.5 and 2, although their negative surface potentials were reduced in magnitude. Our observation of negatively charged polyplexes is consistent with a recent report on RNP delivery by Chen *et al.*[51] This observation of negative surface charge suggests the presence of free RNPs coexisting with weakly bound RNP−polymer complexes, mirroring findings from gel migration assays. Given the high delivery efficiency of P38, it appears that the formation of tightly bound polymer−RNP complexes is not essential for ensuring efficient RNP delivery. At N/P ratios as low as 1, the editing efficiency and toxicity (Figure S23 in the SI) of P38 are comparable to LPF CRISPRMAX and JetCRISPR. This suggests that by minimizing the excess polymer content within polyplexes, we can prevent the formation of strong polymer−RNP interactions that could potentially denature the spCas9 protein, minimize polymer-mediated toxicity, while yet ensuring high levels of delivery efficiency.


https://dx.doi.org/10.1021/acsnano.0c08549
ACS Nano 2020, 14, 17626−17639

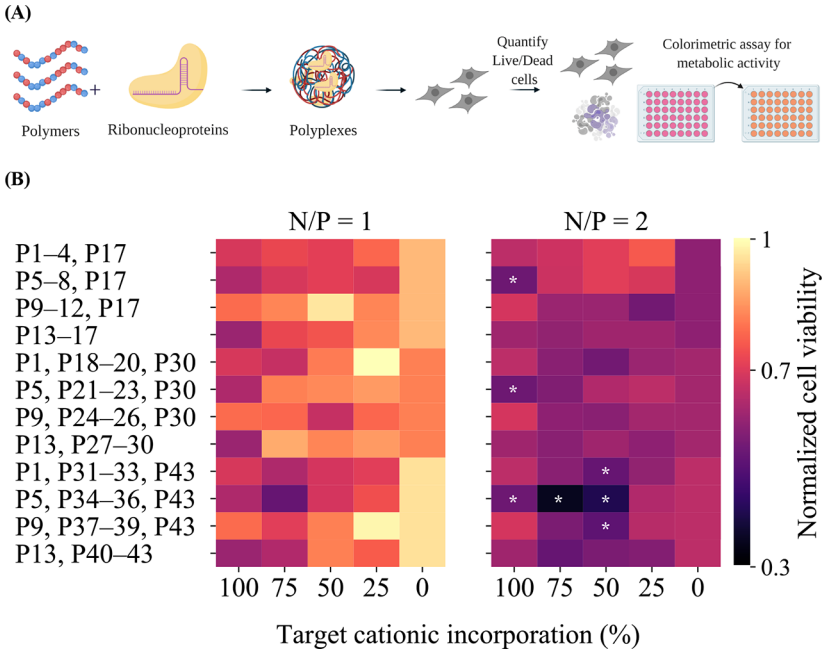


**Figure 7. (A) Cytotoxicity measurements employed the CCK-8 assay. (B) Cellular viability was normalized to that of untreated cells and plotted as a function of polymer composition and N/P ratio. Formulations with the lowest cellular viability (bottom 5 percentile) are highlighted. Six polymers, P5 (highlighted in all three instances), P32, P34, P35, the hit polymer P38, and P40, were identified as the most toxic at higher formulation ratios. Except for P5 (the homopolymer of AEMA), all of them incorporate HEMA as a comonomer.**

Since membrane association, endocytosis, and intracellular trafficking are all size-sensitive phenomena, we performed DLS measurements for the entire library (Figures S12–S14). As for P38, RNPs formulated at N/P ratios of 1 and 2 were around 180 and 240 nm in hydrodynamic radius, which is around 30 times the size of the unpackaged RNP (Figure 6C). The tendency of the hit formulation to form polyplexes larger than 100 nm in radius has interesting implications for cellular internalization and nuclear accumulation.[52] While particles smaller than 100 nm in radius exhibit a preference for clathrin-mediated pathways, larger particles are internalized *via* caveolar pathways, which permit polyplexes to traverse the cytosol and enter the nucleus while avoiding lysosomal interrogation.[19,53] In addition, physical aspects of bolus transfection cannot be overlooked: upon introduction into the cell culture media, bulkier polyplexes will settle to the surface of adherent monolayer cultures faster than smaller polyplexes.[54] The large size of P38 polyplexes may have eliminated the need to improvise endosomal escape routes and imparted favorable transport characteristics that maximized polyplex–cell contact.

Herein, we discovered that (1) binding between the RNP payload and the polymer was incomplete, with a small fraction of RNPs remaining unbound, (2) although the diameter of P38–RNP complexes exceeds the optimal range for *in vitro* delivery, P38 was somehow able to direct RNP payloads along cellular pathways favoring nuclear internalization. Despite these departures from established design heuristics, P38 proved to be an excellent chemically defined vector, with a delivery efficiency far higher than that of commercially available reagents, illustrating the power of the high-throughput approach to deliver efficient polymeric vehicles from underexplored domains in chemical space.

**Cytotoxicity, Cellular Uptake, and Intracellular Payload Distribution.** Combinatorial polymer design and parallelized experimentation rapidly yielded a promising lead structure (P38) that exceeds benchmarks set by commercial PEI and lipid-based reagents for RNP delivery. However, our inability to identify any obvious structural driver of P38's intracellular delivery efficacy prompted us to expand the scope of our investigations beyond editing efficiency to include toxicity and the cellular internalization of RNP payloads. First, we studied how the cellular toxicity originating from polyplex-mediated RNP delivery is shaped by the identity and the degree of incorporation of hydrophilic comonomers, the p$K_a$ of the cationic monomer, N/P ratios, polymer p$K_a$, charge densities, and polymer hydrophobicity. We measured the toxicity associated with each polyplex formulation through CCK-8 assays and plotted responses in the form of a heat map (Figure 7). For most cationic monomers, increasing cationic monomer incorporation was accompanied by higher cytotoxicity, potentially originating from cell membrane disruptions caused by the uptake of cationic polyplexes. At an N/P ratio of 1, the toxicity of P38 is comparable to that of LPF CRISPRMAX and JetCRISPR, while its editing efficiency is higher than that obtained through either commercial reagent (Figure S23 in the SI). We were surprised to discover that P38 was not the only polymer in the library to result in deterioration of cellular viability. Five other polymers (P5, P32, P34, P35, and P40) induced comparable or higher levels of toxicity than P38. Excepting P38, each of these formulations were ineffective at mediating functional RNP delivery during image cytometry screening. In this list of high-toxicity formulations, except for P5 (a homopolymer of AEMA), all polymers were constituted from HEMA, the least hydrophilic comonomer in the library. This underscores the importance of comonomer hydrophilicity and phase behavior in shaping cell–polyplex interactions.

Next, we investigated the relationship between RNP uptake and polyplex composition through a library-wide internalization study. We recognized that while several polyplexes may


https://dx.doi.org/10.1021/acsnano.0c08549
ACS Nano 2020, 14, 17626–17639

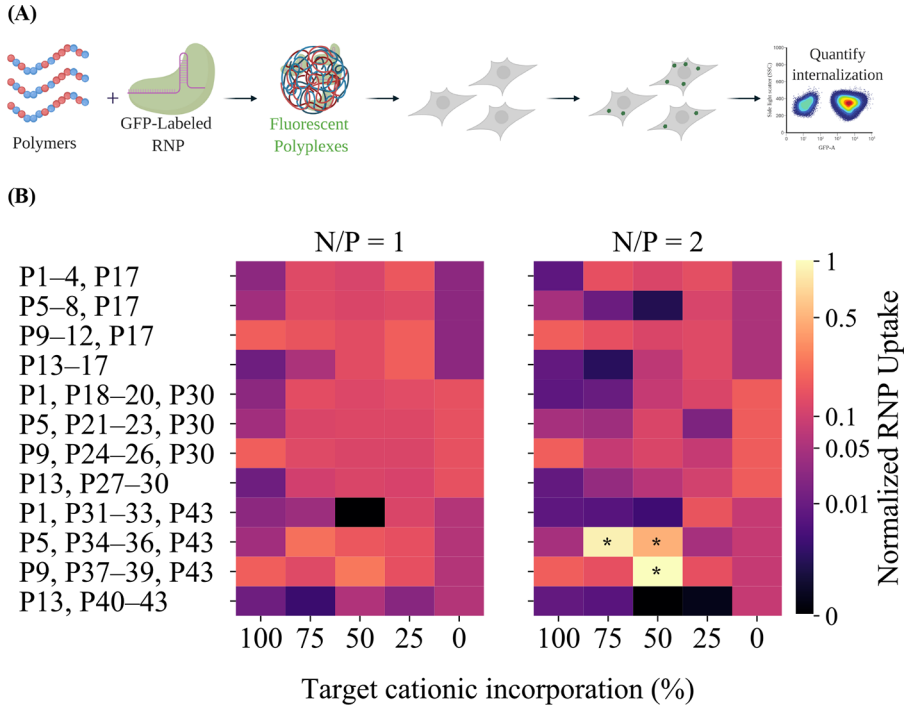


**Figure 8. (A) GFP-labeled RNPs were complexed with each polymer at two N/P ratios. Flow cytometry was used to measure the cellular internalization of the polyplex formulations across the entire library. (B) Cellular uptake of RNPs (geometric mean of GFP intensity was normalized) represented as a function of polymer composition and N/P ratio. Instances of highly efficient internalization are highlighted. The hit polymer, P38, as well as two copolymers from the p(AEMA-*st*-HEMA) series (P34 and P35) displayed the highest cellular uptake.**

be limited by cellular internalization, for some other polyplex formulations, endolysosomal navigation and payload unpackaging might have prohibited RNP release within the cytosol. We hoped to discriminate between instances where low editing efficiency originated merely from poor cellular internalization and instances where intracellular payload delivery was impaired despite high levels of cellular internalization. Annealing sgRNA with a fusion protein of GFP and spCas9, we generated fluorescent RNP variants to quantify the RNP internalization effected by 43 polymers in the library at two N/P ratios (Figure 8A). As expected, P38 polyplexes were internalized most efficiently at both N/P ratios studied, with the majority of the polyplex library resulting in RNP uptake levels comparable to those achieved by uncomplexed or naked payloads (Figure 8B). Surprisingly, two copolymers from the p(AEMA-*st*-HEMA) subfamily (P34 and P35) gave rise to RNP uptake levels comparable to those of P38 (highlighted in the heatmap with black stars). Except for these three structures (P34, P35, and P38), interactions between polyplexes and cell membranes did not culminate in cellular entry, explaining the subpar editing efficiencies that were observed for the majority of the library. Unlike other underperforming polymer candidates, the RNP delivery of P34 and P35 was not compromised by inefficient cellular internalization; rather we suspected that the intracellular trajectories of these two polyplex formulations did not mirror that of P38, consigning them to a different fate.

To examine the subcellular localization of polyplexes, we performed immunofluorescence studies with GFP-labeled RNPs and anti-LAMP2 antibodies that facilitated visualization of lysosomal compartments (Figure 9). We compared the intracellular distribution of labeled RNPs complexed with the hit polymer P38 and the two near-miss polymers, P34 and P35, at an N/P ratio of 2. We observed that all three sets of

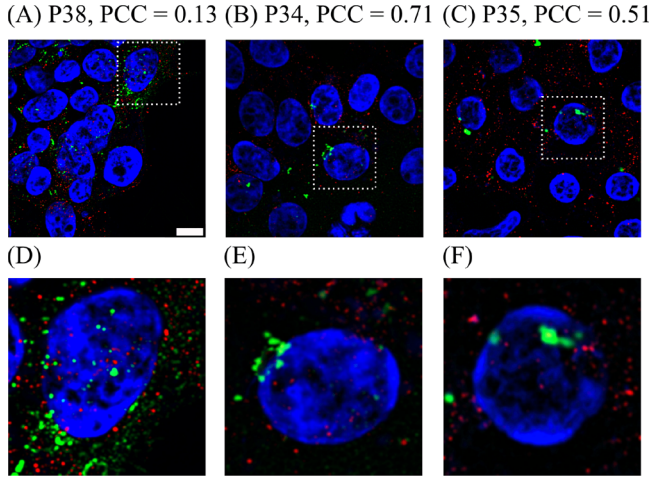


**Figure 9. Representative images, depicting the intracellular distribution of GFP-labeled RNP payloads for (A) the hit polymer P38, as well as the "near miss" polymers, (B) P34 and (C) P35. Lysosomal compartments are visualized in the red channel, nuclei in the blue channel, and GFP-labeled RNP payloads in the green channel. Scale bar is 10 $\mu$m. The Pearson's correlation coefficient (PCC) between the GFP intensities and the fluorescent signal intensities from labeled lysosomes was calculated for each polyplex formulation across four replicates, and the average value reported. (D), (E), and (F) insets show high-magnification views of (A), (B), and (C), respectively.**

polyplexes were successfully internalized, as indicated by the appearance of GFP signals associated with the RNPs. We performed Z-stacked confocal scans (four replicates) for these three treatment groups and quantified the Pearson's correlation coefficient (PCC) between the GFP signals from


https://dx.doi.org/10.1021/acsnano.0c08549
*ACS Nano* 2020, 14, 17626–17639

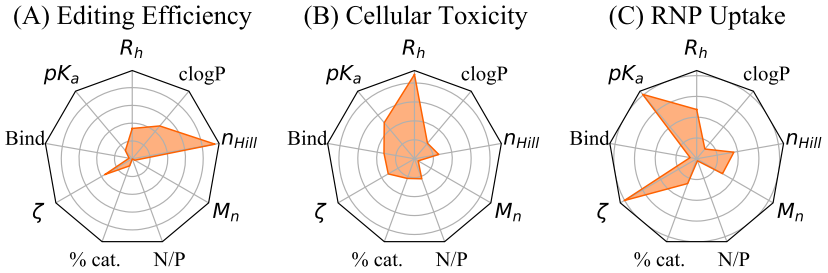


**Figure 10. Random forest classifiers (RFCs) were used to map nine physicochemical descriptors (polyplex radius, polymer hydrophobicity, the Hill coefficient, polymer length, N/P ratio, polymer composition, charge density, RNP binding affinity, and p$K_a$) to (A) editing efficiency, (B) cytotoxicity, and (C) RNP uptake. While editing efficiency is highly dependent on hydrophobicity-associated parameters such as clogP and $n_{Hill}$, toxicity and RNP uptake are determined by polyplex diameter and parameters associated with polycation protonation state (ζ-potential and p$K_a$), respectively.**

labeled RNPs and the red signals from labeled lysosomes using Costes' method.[55] The mean PCC was highest (0.71 ± 0.29) in P34 and lowest in the hit polymer P38 (0.13 ± 0.11), while P35 had a PCC of 0.51 ± 0.33. From colocalization analysis (Figure S25), we found that near-miss polymers P34 and P35 were more likely to colocalize with lysosomal compartments than the hit polymer P38.

**Machine Learning Uncovers Structural Drivers of Cytotoxicity, Cellular Uptake, and Editing Efficiency.** From our library-wide evaluation of toxicity and RNP internalization, we discovered that P38 was not the sole polymer to effect high cellular internalization of RNP payloads or perturb cellular health. Yet, P38 alone achieved efficient genome editing, suggesting that the structural determinants underlying editing efficiency, toxicity, and internalization are not identical. We turned to data science techniques to elucidate the surprising contrasts in delivery performance between P38 and the rest of the library. Did a single dominant design attribute mark P38 out for success or did multiple polyplex attributes act in concert? What are the design attributes shared by P38 and the near-miss polymers that resulted in high RNP uptake? Why did our near-miss polymers exhibit a cellular internalization rate comparable to P38 and yet fail to deliver RNP payloads efficiently? Since intuition-based methods of pattern recognition failed to answer these questions, we applied random forest classifiers (RFC) on data sets comprising measurements of RNP delivery, toxicity, and uptake.

We included nine polymer descriptors in our analysis, of which seven were derived routinely: polymer composition (abbreviated as % cat.), polymer length ($M_n$), the N/P ratio, the p$K_a$ (Figure S10), and ζ-potential values of the polymers in their unbound state in PBS (Table 1), the polyplex hydrodynamic radius ($R_h$, Figures S12–S14), and qualitatively determined RNP binding affinities (Figures S15–S17). To account for hydrophobicity, we employed fragment-based approaches[56,57] to estimate the octanol–water partition coefficients of oligomeric approximations (10-mers) of our polymers through clogP calculations. Finally, we quantified the cooperativity during hydrophobically driven polymer deprotonation by computing the Hill coefficient ($n_{Hill}$) from p$K_a$ titration curves using the approach reported by Li *et al.*[58] (Figure S11 and Table S5 in the SI).

Three RFCs were trained on the editing efficiency, cellular toxicity, and RNP uptake data sets, respectively. To build RFCs, we constructed ensembles of "decision trees", wherein each decision tree examines small cross sections of the data set using randomly selected subsets of the nine physicochemical descriptors to classify each polymer according to the criteria specified: (1) not a hit/hit (normalized mCherry is greater than 0.4), (2) less toxic/toxic (criterion: bottom five percentile of cellular viability), and (3) low/high RNP uptake (geometric mean of GFP fluorescent intensity is less than 30% of that observed with the lead structure P38). Randomization of both data points and descriptors ensures that the classification rules developed by each decision tree are diverse, that multiple explanations are considered, and that we obtain a representative picture of the underlying patterns in the data. By quantifying the reliance of decision trees on these nine descriptors during classification tasks, we calculated the feature importance of each descriptor in determining editing efficiency, cellular toxicity, and RNP uptake.

We visualized feature importance across these three biological readouts in the form of a radar plot (Figure 10) and observed striking differences. While hydrophobicity-linked parameters such as clogP and $n_{Hill}$ were the primary structural drivers of editing efficiency, polyplex size ($R_h$) and polymer charge density (ζ-potential) also contributed substantially. Although hydrophobicity enhancement has frequently been touted as a potent design strategy essential to achieve efficient payload delivery,[22,23,39,59,60] no study has previously examined the role of hydrophobically driven cooperative deprotonation in enhancing nucleic acid delivery. Wu *et al.*[61] recently reported that chemotherapeutic drug combinations with elevated dose–response Hill coefficients displayed the highest antitumoral activity.[61] Li *et al.*[58] demonstrated that when polymer hydrophobicity exceeds a certain threshold, phase separation caused by the hydrophobic collapse of deprotonated polymer segments drives further deprotonation, triggering a highly cooperative deprotonation process among polymers with high Hill coefficients. We speculate that polymers such as P38, which are characterized by high $n_{Hill}$ values, unpackage their payloads more rapidly within the cytosol compared to those with low $n_{Hill}$. In the case of cellular toxicity and RNP uptake, clogP and $n_{Hill}$ had negligible impact. Polyplex diameter and polymer p$K_a$ were the most influential structural determinants of cellular toxicity, with bulkier polyplexes resulting in severe toxicity. In fact, the five polyplex formulations identified as toxic in Figure 7B (P5, P32, P34, P35, and P40) possessed both large hydrodynamic radii (200–500 nm) and high values of p$K_a$ (greater than 7.2). We attributed the size-dependence of polyplex-mediated cytotoxicity to higher frequencies of polyplex–cell contacts resulting from faster settling velocities of bulkier polyplexes during bolus


https://dx.doi.org/10.1021/acsnano.0c08549
ACS Nano 2020, 14, 17626–17639

transfection.[62] As for RNP uptake, polymers with higher values of p$K_a$ and $\zeta$-potential were more adept at gaining cellular entry, possibly through electrostatically mediated interactions with the negatively charged cell membrane. This finding is consistent with previous reports that elevated surface charge density and high degree of protonation can promote nonspecific cellular uptake of polyplexes.[63−67]

From the examples of the near-miss polymers P34 and P35, it is apparent that promoting polycation protonation and maximizing polycation charge density can enhance cellular uptake of RNPs; however, such structures may still prove to be ineffectual in releasing payloads within the cytosol if they do not satisfy the design constraints for clogP and $n_{Hill}$. To mediate efficient intracellular unpackaging, we must maximize clogP and the Hill coefficient by incorporating co-monomers of moderate hydrophilicity and tertiary amines with bulky hydrophobic substituents, while avoiding extremely hydrophilic monomers such as PEG and zwitterionic moieties. We eschewed univariate analysis in favor of a machine learning approach that examined nine polymer descriptors and ultimately discovered a subset of descriptors that were most predictive of editing efficiency and toxicity. This allowed us to identify the most influential polymer descriptors associated with each biological response in an unbiased manner.

## CONCLUSIONS

We adopted parallelized experimental workflows and combinatorial polymer design to efficiently explore a multivariate polycation design space. Combinatorial design allowed us to create a chemically diverse polymer library and access a wide range of polymer physicochemical properties. Through parallelized experimentation, we acquired an extensive suite of physicochemical characterization data consisting of polymer composition, molecular weight distribution, p$K_a$, polyplex size distribution, RNP binding affinity, charge density, and key biological readouts such as cellular toxicity, RNP uptake, and RNP delivery efficiency. Image cytometry identified a hit polymer within this chemical space (P38), which outperformed all four commercial RNP delivery reagents that it was benchmarked against. Sanger sequencing was applied to analyze indel formation during NHEJ editing, and these unambiguous estimates of editing efficiency validated our conclusions from image cytometry. With an editing efficiency of 58%, which is twice that of JetCRISPR and Lipofectamine CRISPRMAX, P38 is an exciting prospect for nonviral *ex vivo* gene editing. To identify the physicochemical basis underlying the RNP delivery capabilities of P38, we examined correlations between polymer structure, properties, and biological performance. A library-wide evaluation of editing efficiency, cellular viability, and internalization formed the basis for machine learning models that captured key biophysical trends. Although polyplex aggregation and polycation protonation equilibria drive cellular toxicity and RNP uptake respectively, RNP unpackaging and functional intracellular delivery will be achieved only by engineering hydrophobic polycations that deprotonate cooperatively. We applied data science tools to identify physicochemical determinants of payload delivery, cellular uptake, and toxicity, thereby providing polymer chemists with valuable experimental guidance to tailor vector properties to meet varied clinical objectives. By extending this powerful methodology across diverse cell types and nucleic acid modalities, we will establish an efficient discovery pipeline for synthetic vectors whose properties can be tailored on demand to fulfill a multitude of therapeutic *ex vivo* and *in vivo* applications.

## METHODS AND MATERIALS

**Polymer Synthesis and Purification.** All reagents were purchased from Sigma-Aldrich except for 4-cyano-4-[(ethylsulfanylthiocarbonyl)sulfanyl]pentanoic acid (CEP), which was purchased from Asta Tech (China) and used without further purification. RAFT polymerization was performed in the Carousel 12 parallel synthesizer (Radleys, UK), which enables the completion of 12 RAFT reactions in parallel. The quantities of chain-transfer agent (CTA), initiator, monomers, and the solvents dispensed are specified in Table S1 in the SI. After addition of the desired quantities of monomer, CTA, initiator, and solvent, all reaction modules were simultaneously degassed using three or four freeze−pump−thaw cycles, heated to a temperature of 78 °C, and stirred overnight under an inert $N_2$ environment. Eighteen hours later, the reaction mass was quenched and an equal volume of 1 N HCl added. Polymer purification was performed through dialysis. Dialysis membranes with a molecular weight cutoff of 3000 Da (Spectrum Chemicals, NJ, USA) were used. Polymers were dialyzed over 3 days in acidified water that was replaced twice daily. Finally, lyophilization (SP Scientific, PA, USA) was performed for 2 days, yielding pure polymers.

**Polymer Characterization.** NMR was performed on the Bruker Avance III HD 500 instrument. A total of 32 scans were acquired using a relaxation time of 10 seconds. Size exclusion chromatography (Agilent, CA, USA) was performed using refractive index and multiple-angle light-scattering detectors (Wyatt, Santa Barbara, CA, USA) to determine the complete molecular weight distribution for all copolymers. An automated titrator, Orion Star T901 pH titrator (Thermo Fisher, Waltham, MA, USA) was employed for p$K_a$ determination, with an initial polymer concentration of 0.5 mg/mL. The Zetasizer (Malvern Instruments, MA, USA) was used to evaluate the $\zeta$-potential of polymers dissolved in PBS, with three to five replicates each.

**Physical Characterization of Polyplexes.** Synthetic single guide RNA (100 bp) was synthesized with a sequence of GCACCUAUAGAUUACUAUCCGUUUUAGAGCUAGAAAUAG-CAAGUUAAAAUAAGGCUAGUCCGUUAUCAACUUGAAAAA-GUGGCACCGAGUCGGUGCUUUU (Synthego, CA, USA). The spCas9 protein was ordered from Aldveron, ND, USA. Polymer stock solutions were prepared in PBS at a concentration of 1 mg/mL, sterile-filtered, and further diluted in PBS to achieve targeted N/P ratios. Ribonucleoproteins were assembled by adding sgRNA (0.039 and 0.05 mg/mL for DLS and gel migration, respectively) to equal volumes of Cas9 protein (0.19 and 0.25 mg/mL for DLS and gel migration respectively), obtaining a 1:1 molar mixture. Both sgRNA and spCas9 stock solutions were diluted in PBS to obtain desired concentrations. RNP complexes were annealed for 10−15 min at room temperature. Then, equal volumes of diluted polymer solutions were added to form polyplexes. Polyplexes were maintained at ambient temperature for 45 min prior to DLS or gel migration studies.

Gel casting was completed using 1.5% w/v agarose solutions in TAE buffer. To visualize sgRNA bands, ethidium bromide was used at a concentration of 0.017% v/v. Electrophoresis was performed at 80 V over 60 min and imaged using a transilluminator (Fotodyne, IL, USA) under UV light. For DLS, the DynaPro plate reader III (Wyatt Instruments, CA, USA) was used, and three to five replicates were performed. For electrokinetic characterization of polyplexes, the sgRNA concentration was fixed at 0.05 mg/mL and the spCas9 concentration at 0.25 mg/mL. Three to five measurements were collected per sample using the Zetasizer (Malvern Instruments, MA, USA).

**Biological Assays.** The HEK293 cell line engineered with a traffic light reporter system[49] was used to assess RNP delivery. To obtain a stable cell line, subcloning was performed at the Genome Engineering Shared Resource (Minneapolis, MN, USA). Cells were maintained in DMEM supplemented with 10% heat-inactivated fetal bovine serum


https://dx.doi.org/10.1021/acsnano.0c08549
ACS Nano 2020, 14, 17626−17639

(Thermo Fisher) at 37 °C and 5% $CO_2$ in 75 $cm^2$ cell culture flasks. All polymer stock solutions were formulated at a concentration of 1 mg/mL and sterile filtered. The spCas9 protein (Aldevron, ND, USA) and sgRNA (Synthego, CA, USA) solutions were prepared at concentrations of 0.039 and 0.19 mg/mL, respectively, in PBS. Ribonucleoproteins were formed by addition of sgRNA to spCas9 and annealing for 15 min. Thereafter equal volumes of diluted polymer solutions were added to the RNP to achieve desired N/P ratios. Polyplexes were diluted in OptiMEM before introducing them to the cells. For 24-well plates, a nucleic acid loading of 1 $\mu$g/mL sgRNA was employed. Manufacturer's protocols were executed for commercial reagents. Image cytometry was performed in FluorBrite (Thermo Fisher), and cells were stained by adding 1 drop of Nucelobrite (Thermo Fisher) to each well to visualize nuclear outlines and facilitate cell counting. Live cell imaging was performed using the Zeiss Cell Observer (Zeiss AG, Switzerland) equipped with a motorized stage, environmental control chamber, and automated image acquisition features. Images were analyzed using Cell profiler using previously detailed procedures.[62]

For flow cytometric measurements of mCherry, cells were stained with a Calcein violet viability marker, and the 405 and 560 nm laser lines were used on the ZE5 (Biorad, Inc., CA, USA). Single live cells were used for analysis, and gating schemes are furnished in Figure S21. At least 80 000 events were collected for every treatment condition, and three technical replicates were performed. For sequencing, the DNA of transfected cells was extracted using QuickExtract DNA extraction solution (Lucigen, WI, USA), according to the manufacturer's protocol. PCR amplification was completed using the AccuPrime Taq DNA Polymerase kit (Thermo Fisher), in accordance with the PCR protocol recommended by the manufacturer. Primer sequences used were 5′ AGACCACCC-CCATGTACAAA 3′ and 5′ GGAAAACCCTTCCTGGTTTC 3′. Primers were ordered from Integrated DNA Technologies (IDT, Skokie, IL, USA) and dissolved in ultrapure water. Subsequent to PCR, amplified products were purified using gel electrophoresis in 1 wt % agarose gel. Excised gel fragments were further purified using a Monarch DNA gel extraction kit (New England BioLabs, MA). Purified DNA products were eluted in ultrapure water and analyzed using Sanger sequencing (University of Minnesota Genomics Center, Twin Cities Campus) after the addition of primer.

For cytotoxicity, cell culture media was replaced with a 2% solution of CCK-8 (Dojindo) in Fluorbrite 2 days after transfection. Thereafter, cells were incubated for 4 h and absorbance was measured at 450 nm using the Synergy H1 plate reader (Biotek, CA, USA). Measurements of the CCK-8 solution placed in empty wells were collected, and this blank reading was subtracted from all data points. Absorbance values were normalized to untreated cells. Six wells were employed per treatment group. For uptake studies, GFP-labeled Cas9 (Thermo Fisher catalog no. CAS9GFPPRO-250UG) was used to formulate RNPs. Twenty-four hours after polyplexes were administered, cells were incubated with CellScrub (Genlantis, San Diego, CA, USA) at room temperature for 10 min and washed again with PBS to remove extracellularly bound RNPs. For confocal imaging, cells were plated on sterilized gelatin-coated glass coverslips in 24-well plates a day before transfection. A day after transfection, cells were fixed *via* immersion fixation, and immunofluorescent labeling of lysosomes was completed with the anti-LAMP2 primary antibody (Abcam catalog no. ab25631, Cambridge, MA, USA) and a secondary antibody (Invitrogen catalog no. A11003) diluted to 1:200 and 1:1000, respectively. Antibodies were diluted in a solution of PBS containing 5% bovine serum albumin, 0.2% gelatin, and 0.1% Triton-X. Cells were counterstained with Hoechst 3342, and three washing steps of 5 min each were performed with PBS/0.1% Triton-X after each antibody incubation step. Coverslips were mounted on Prolong Glass (Thermo Fisher) and cured at room temperature in the dark for 2 days. Samples were imaged under an Olympus BX2 laser-scanning confocal microscope system equipped with an automated upright BX61 microscope base and a PRIOR ProScanII motorized stage. Colocalization of green and red signals was assessed with the ImarisColoc module in Imaris 9.2.0 (b47084) software (Bitplane AG, Zurich, Switzerland). Pearson's correlation coefficients were calculated for colocalized image volumes across four images within each treatment group to obtain mean PCC values.

**Identification of Structure−Function Relationships through Machine Learning.** Random forest classifiers were trained on nine descriptors in order to classify cellular uptake, toxicity, and editing efficiency under high/low categories for a given polyplex formulation. The data set consisted of 86 rows with nine descriptor columns for each of the three response variables (toxicity, uptake, and efficiency). Our modeling workflow is described in detail in section 11 in the SI. Briefly, hyperparameter tuning was performed using GridsearchCV and three cross-validation folds. A training-test split of 60−40% was employed. We have reported model performance metrics in the form of accuracy, precision, recall, and ROC-AUC (area under the curve of receiver operating characteristic curves) scores in Table S4 in the SI. The scikit-learn library in Python was used for all computations. The Python scripts used to identify the structure−function relationships reported her as well as the raw data are available from the corresponding author upon reasonable request.

## ASSOCIATED CONTENT

### Supporting Information

The Supporting Information is available free of charge at https://pubs.acs.org/doi/10.1021/acsnano.0c08549.

Detailed experimental procedures, statistical modeling workflows, supplemental data from flow cytometry, NMR, p$K_a$ titrations, DLS, gel migration, sequencing, confocal imaging, and colocalization analyses (PDF)

## AUTHOR INFORMATION


### Corresponding Author

**Theresa M. Reineke** − *Department of Chemistry, University of Minnesota, Minneapolis, Minnesota 55455, United States;* orcid.org/0000-0001-7020-3450; Email: treineke@umn.edu

### Authors

**Ramya Kumar** − *Department of Chemistry, University of Minnesota, Minneapolis, Minnesota 55455, United States;* orcid.org/0000-0002-8725-0023

**Ngoc Le** − *Department of Chemistry, University of Minnesota, Minneapolis, Minnesota 55455, United States*

**Zhe Tan** − *Department of Chemistry, University of Minnesota, Minneapolis, Minnesota 55455, United States;* orcid.org/0000-0002-3518-0772

**Mary E. Brown** − *University Imaging Centers, University of Minnesota, Minneapolis, Minnesota 55455, United States*

**Shan Jiang** − *Department of Chemistry, University of Minnesota, Minneapolis, Minnesota 55455, United States*

Complete contact information is available at: https://pubs.acs.org/10.1021/acsnano.0c08549


### Notes

The authors declare no competing financial interest.

## ACKNOWLEDGMENTS

We thank Guillermo Marques, Ph.D. (University of Minnesota, University Imaging Centers), and Thomas Pengo, Ph.D. (University of Minnesota Informatics Institute), for technical advice and consultation. We acknowledge the Defense Advanced Research Projects Agency (DARPA) for funding provided under contract number N660011824041. This work was supported partially by the National Science Foundation through the University of Minnesota MRSEC under Award

No. DMR-2011401. We also acknowledge Limelight Bio for partial support. R.K. acknowledges Biorender.com for figure preparation.

## REFERENCES

(1) Doudna, J. A.; Charpentier, E. The New Frontier of Genome Engineering with CRISPR-Cas9. *Science* **2014**, *346*, 1258096.
(2) Doudna, J. A. The Promise and Challenge of Therapeutic Genome Editing. *Nature* **2020**, *578*, 229−236.
(3) Zipkin, M. CRISPR's "Magnificent Moment" in the Clinic. *Nat. Biotechnol.* **2019**, DOI: 10.1038/d41587-019-00035-2
(4) Cross, R. *Custom CRISPR Therapies Could Be Closer than You Think*. https://cen.acs.org/business/Custom-CRISPR-therapies-closer-be-closer-than-you-think/97/web/2019/10.
(5) Sheridan, C. Go-Ahead for First In-Body CRISPR Medicine Testing. *Nat. Biotechnol.* **2018**, DOI: 10.1038/d41587-018-00003-2.
(6) The First U.S. Trials in People Put CRISPR to the Test in 2019. *Science News*. https://www.sciencenews.org/article/crispr-gene-editor-human-clinical-trials-top-science-stories-2019-yir.
(7) Lostalé-Seijo, I.; Montenegro, J. Synthetic Materials at the Forefront of Gene Delivery. *Nature Reviews Chemistry* **2018**, *2*, 258−277.
(8) Wilbie, D.; Walther, J.; Mastrobattista, E. Delivery Aspects of CRISPR/Cas for *in Vivo* Genome Editing. *Acc. Chem. Res.* **2019**, *52*, 1555−1564.
(9) Li, L.; He, Z. Y.; Wei, X. W.; Gao, G. P.; Wei, Y. Q. Challenges in CRISPR/CAS9 Delivery: Potential Roles of Nonviral Vectors. *Hum. Gene Ther.* **2015**, *26*, 452−462.
(10) Xu, C. L.; Ruan, M. Z. C.; Mahajan, V. B.; Tsang, S. H. Viral Delivery Systems for CRISPR. *Viruses* **2019**, *11*, 28.
(11) Liu, C.; Zhang, L.; Liu, H.; Cheng, K. Delivery Strategies of the CRISPR-Cas9 Gene-Editing System for Therapeutic Applications. *J. Controlled Release* **2017**, *266*, 17−26.
(12) Wang, H.-X.; Li, M.; Lee, C. M.; Chakraborty, S.; Kim, H.-W.; Bao, G.; Leong, K. W. CRISPR/Cas9-Based Genome Editing for Disease Modeling and Therapy: Challenges and Opportunities for Nonviral Delivery. *Chem. Rev.* **2017**, *117*, 9874−9906.
(13) Putnam, D. Polymers for Gene Delivery across Length Scales. *Nat. Mater.* **2006**, *5*, 439−451.
(14) Pack, D. W.; Hoffman, A. S.; Pun, S.; Stayton, P. S. Design and Development of Polymers for Gene Delivery. *Nat. Rev. Drug Discovery* **2005**, *4*, 581−593.
(15) Yin, H.; Kauffman, K. J.; Anderson, D. G. Delivery Technologies for Genome Editing. *Nat. Rev. Drug Discovery* **2017**, *16*, 387−399.
(16) Eoh, J.; Gu, L. Biomaterials as Vectors for the Delivery of CRISPR−Cas9. *Biomater. Sci.* **2019**, *7*, 1240−1261.
(17) Sun, H.; Yang, L.; Thompson, M. P.; Schara, S.; Cao, W.; Choi, W.; Hu, Z.; Zang, N.; Tan, W.; Gianneschi, N. C. Recent Advances in Amphiphilic Polymer−Oligonucleotide Nanomaterials *via* Living/Controlled Polymerization Technologies. *Bioconjugate Chem.* **2019**, *30*, 1889−1904.
(18) Vermeulen, L. M.; De Smedt, S. C.; Remaut, K.; Braeckmans, K. The Proton Sponge Hypothesis: Fable or Fact? *Eur. J. Pharm. Biopharm.* **2018**, *129*, 184−190.
(19) Pichon, C.; Billiet, L.; Midoux, P. Chemical Vectors for Gene Delivery: Uptake and Intracellular Trafficking. *Curr. Opin. Biotechnol.* **2010**, *21*, 640−645.
(20) Ong, Z. Y.; Yang, C.; Cheng, W.; Voo, Z. X.; Chin, W.; Hedrick, J. L.; Yang, Y. Y. Biodegradable Cationic Poly(carbonates): Effect of Varying Side Chain Hydrophobicity on Key Aspects of Gene Transfection. *Acta Biomater.* **2017**, *54*, 201−211.
(21) Piest, M.; Engbersen, J. F. Effects of Charge Density and Hydrophobicity of Poly(amido Amine)s for Non-Viral Gene Delivery. *J. Controlled Release* **2010**, *148*, 83−90.
(22) Nelson, C. E.; Kintzing, J. R.; Hanna, A.; Shannon, J. M.; Gupta, M. K.; Duvall, C. L. Balancing Cationic and Hydrophobic Content of PEGylated siRNA Polyplexes Enhances Endosome Escape, Stability, Blood Circulation Time, and Bioactivity *in Vivo*. *ACS Nano* **2013**, *7*, 8870−8880.
(23) Werfel, T. A.; Jackson, M. A.; Kavanaugh, T. E.; Kirkbride, K. C.; Miteva, M.; Giorgio, T. D.; Duvall, C. Combinatorial Optimization of PEG Architecture and Hydrophobic Content Improves Ternary siRNA Polyplex Stability, Pharmacokinetics, and Potency *in Vivo*. *J. Controlled Release* **2017**, *255*, 12−26.
(24) Zhu, D.; Yan, H.; Zhou, Z.; Tang, J.; Liu, X.; Hartmann, R.; Parak, W. J.; Feliu, N.; Shen, Y. Detailed Investigation on How the Protein Corona Modulates the Physicochemical Properties and Gene Delivery of Polyethylenimine (PEI) Polyplexes. *Biomater. Sci.* **2018**, *6*, 1800−1817.
(25) Pezzoli, D.; Giupponi, E.; Mantovani, D.; Candiani, G. Size Matters for *in Vitro* Gene Delivery: Investigating the Relationships among Complexation Protocol, Transfection Medium, Size and Sedimentation. *Sci. Rep.* **2017**, *7*, 1−11.
(26) Alabi, C. A.; Love, K. T.; Sahay, G.; Yin, H.; Luly, K. M.; Langer, R.; Anderson, D. G. Multiparametric Approach for the Evaluation of Lipid Nanoparticles for siRNA Delivery. *Proc. Natl. Acad. Sci. U. S. A.* **2013**, *110*, 12881−12886.
(27) Li, Y.; Yang, T.; Yu, Y.; Shi, N.; Yang, L.; Glass, Z.; Bolinger, J.; Finkel, I. J.; Li, W.; Xu, Q. Combinatorial Library of Chalcogen-Containing Lipidoids for Intracellular Delivery of Genome-Editing Proteins. *Biomaterials* **2018**, *178*, 652−662.
(28) Li, Y.; Bolinger, J.; Yu, Y.; Glass, Z.; Shi, N.; Yang, L.; Wang, M.; Xu, Q. Intracellular Delivery and Biodistribution Study of CRISPR/Cas9 Ribonucleoprotein Loaded Bioreducible Lipidoid Nanoparticles. *Biomater. Sci.* **2019**, *7*, 596−606.
(29) Billingsley, M. M.; Singh, N.; Ravikumar, P.; Zhang, R.; June, C. H.; Mitchell, M. J. Ionizable Lipid Nanoparticle-Mediated mRNA Delivery for Human CAR T Cell Engineering. *Nano Lett.* **2020**, *201578*.
(30) Kuhn, J.; Lin, Y.; Krhac Levacic, A.; Al Danaf, N.; Peng, L.; Höhn, M.; Lamb, D. C.; Wagner, E.; Lächelt, U. Delivery of Cas9/sgRNA Ribonucleoprotein Complexes *via* Hydroxystearyl Oligoamino Amides. *Bioconjugate Chem.* **2020**, *31*, 729.
(31) Ramishetti, S.; Hazan-Halevy, I.; Palakuri, R.; Chatterjee, S.; Naidu Gonna, S.; Dammes, N.; Freilich, I.; Kolik Shmuel, L.; Danino, D.; Peer, D. A Combinatorial Library of Lipid Nanoparticles for RNA Delivery to Leukocytes. *Adv. Mater.* **2020**, *32*, 1906128.
(32) Lynn, D. M.; Anderson, D. G.; Putnam, D.; Langer, R. Accelerated Discovery of Synthetic Transfection Vectors: Parallel Synthesis and Screening of a Degradable Polymer Library. *J. Am. Chem. Soc.* **2001**, *123*, 8155−8156.
(33) Akinc, A.; Lynn, D. M.; Anderson, D. G.; Langer, R. Parallel Synthesis and Biophysical Characterization of a Degradable Polymer Library for Gene Delivery. *J. Am. Chem. Soc.* **2003**, *125*, 5316−5323.
(34) Anderson, D. G.; Lynn, D. M.; Langer, R. Semi-Automated Synthesis and Screening of a Large Library of Degradable Cationic Polymers for Gene Delivery. *Angew. Chem., Int. Ed.* **2003**, *42*, 3153−3158.
(35) Green, J. J.; Zugates, G. T.; Tedford, N. C.; Huang, Y. H.; Griffith, L. G.; Lauffenburger, D. A.; Sawicki, J. A.; Langer, R.; Anderson, D. G. Combinatorial Modification of Degradable Polymers Enables Transfection of Human Cells Comparable to Adenovirus. *Adv. Mater.* **2007**, *19*, 2836−2842.
(36) Anderson, D. G.; Akinc, A.; Hossain, N.; Langer, R. Structure/Property Studies of Polymeric Gene Delivery Using a Library of Poly(β-Amino Esters). *Mol. Ther.* **2005**, *11*, 426−434.
(37) Sunshine, J. C.; Akanda, M. I.; Li, D.; Kozielski, K. L.; Green, J. J. Effects of Base Polymer Hydrophobicity and End-Group Modification on Polymeric Gene Delivery. *Biomacromolecules* **2011**, *12*, 3592−3600.
(38) Rinkenauer, A. C.; Vollrath, A.; Schallon, A.; Tauhardt, L.; Kempe, K.; Schubert, S.; Fischer, D.; Schubert, U. S. Parallel High-Throughput Screening of Polymer Vectors for Nonviral Gene Delivery: Evaluation of Structure-Property Relationships of Transfection. *ACS Comb. Sci.* **2013**, *15*, 475−482.

(39) Yan, H.; Zhu, D.; Zhou, Z.; Liu, X.; Piao, Y.; Zhang, Z.; Liu, X.; Tang, J.; Shen, Y. Facile Synthesis of Semi-Library of Low Charge Density Cationic Polyesters from Poly(alkylene Maleate)s for Efficient Local Gene Delivery. *Biomaterials* **2018**, *178*, 559−569.
(40) Jiang, Y.; Lu, Q.; Wang, Y.; Xu, E.; Ho, A.; Singh, P.; Wang, Y.; Jiang, Z.; Yang, F.; Tietjen, G. T.; Cresswell, P.; Saltzman, W. M. Quantitating Endosomal Escape of a Library of Polymers for mRNA Delivery. *Nano Lett.* **2020**, *20*, 1117−1123.
(41) Lee, K.; Conboy, M.; Park, H. M.; Jiang, F.; Kim, H. J.; Dewitt, M. A.; Mackley, V. A.; Chang, K.; Rao, A.; Skinner, C.; Shobha, T.; Mehdipour, M.; Liu, H.; Huang, W. C.; Lan, F.; Bray, N. L.; Li, S.; Corn, J. E.; Kataoka, K.; Doudna, J. A.; et al. Nanoparticle Delivery of Cas9 Ribonucleoprotein and Donor DNA *in Vivo* Induces Homology-Directed DNA Repair. *Nat. Biomed. Eng.* **2017**, *1*, 889−901.
(42) Lee, B.; Lee, K.; Panda, S.; Gonzales-Rojas, R.; Chong, A.; Bugay, V.; Park, H. M.; Brenner, R.; Murthy, N.; Lee, H. Y. Nanoparticle Delivery of CRISPR Into the Brain Rescues a Mouse Model of Fragile X Syndrome From Exaggerated Repetitive Behaviours. *Nat. Biomed. Eng.* **2018**, *2*, 497−507.
(43) Fong, T. C.; Bodovitz, S. Polymer Nanoparticles: Potential for Efficient, Biodegradable, and Cost-Effective Delivery of Gene Therapy to Multiple Tissues. *Cell Gene Ther. Insights* **2020**, *6*, 583−590.
(44) Freitag, F.; Wagner, E. Optimizing Synthetic Nucleic Acid and Protein Nanocarriers: The Chemical Evolution Approach. *Adv. Drug Delivery Rev.* **2020**, DOI: 10.1016/j.addr.2020.03.005.
(45) Sunshine, J. C.; Akanda, M. I.; Li, D.; Kozielski, K. L.; Green, J. J. Effects of Base Polymer Hydrophobicity and End-Group Modification on Polymeric Gene Delivery. *Biomacromolecules* **2011**, *12*, 3592−3600.
(46) Bodnarchuk, M. S.; Doncom, K. E.; Wright, D. B.; Heyes, D. M.; Dini, D.; O'Reilly, R. K. Polyelectrolyte pKa from Experiment and Molecular Dynamics Simulation. *RSC Adv.* **2017**, *7*, 20007−20014.
(47) Murmiliuk, A.; Košovan, P.; Janata, M.; Procházka, K.; Uhlík, F.; Štěpánek, M. Local pH and Effective $pK_a$ of a Polyelectrolyte Chain: Two Names for One Quantity? *ACS Macro Lett.* **2018**, *7*, 1243−1247.
(48) Nová, L.; Uhlík, F.; Košovan, P. Local pH and Effective $pK_a$ of Weak Polyelectrolytes-Insights from Computer Simulations. *Phys. Chem. Chem. Phys.* **2017**, *19*, 14376−14387.
(49) Certo, M. T.; Ryu, B. Y.; Annis, J. E.; Garibov, M.; Jarjour, J.; Rawlings, D. J.; Scharenberg, A. M. Tracking Genome Engineering Outcome at Individual DNA Breakpoints. *Nat. Methods* **2011**, *8*, 671−676.
(50) Steyer, B.; Carlson-Stevermer, J.; Angenent-Mari, N.; Khalil, A.; Harkness, T.; Saha, K. High Content Analysis Platform for Optimization of Lipid Mediated CRISPR-Cas9 Delivery Strategies in Human Cells. *Acta Biomater.* **2016**, *34*, 143−158.
(51) Chen, G.; Abdeen, A. A.; Wang, Y.; Shahi, P. K.; Robertson, S.; Xie, R.; Suzuki, M.; Pattnaik, B. R.; Saha, K.; Gong, S. A Biodegradable Nanocapsule Delivers a Cas9 Ribonucleoprotein Complex for *in Vivo* Genome Editing. *Nat. Nanotechnol.* **2019**, *14*, 974−980.
(52) Degors, I. M. S.; Wang, C.; Rehman, Z. U.; Zuhorn, I. S. Carriers Break Barriers in Drug Delivery: Endocytosis and Endosomal Escape of Gene Delivery Vectors. *Acc. Chem. Res.* **2019**, *52*, 1750−1760.
(53) Rejman, J.; Oberle, V.; Zuhorn, I. S.; Hoekstra, D. Size-Dependent Internalization of Particles *via* the Pathways of Clathrin- And Caveolae-Mediated Endocytosis. *Biochem. J.* **2004**, *377*, 159−169.
(54) Khalil, I. A.; Kogure, K.; Akita, H.; Harashima, H. Uptake Pathways and Subsequent Intracellular Trafficking in Nonviral Gene Delivery. *Pharmacol. Rev.* **2006**, *58*, 32−45.
(55) Costes, S. V.; Daelemans, D.; Cho, E. H.; Dobbin, Z.; Pavlakis, G.; Lockett, S. Automatic and Quantitative Measurement of Protein-Protein Colocalization in Live Cells. *Biophys. J.* **2004**, *86*, 3993−4003.
(56) Mannhold, R.; Poda, G. I.; Ostermann, C.; Tetko, I. V. Calculation of Molecular Lipophilicity: State-of-the-Art and Comparison of Log P Methods on More Than 96,000 Compounds. *J. Pharm. Sci.* **2009**, *98*, 861−893.
(57) Stubbs, C.; Murray, K. A.; Ishibe, T.; Mathers, R. T.; Gibson, M. I. Combinatorial Biomaterials Discovery Strategy to Identify New Macromolecular Cryoprotectants. *ACS Macro Lett.* **2020**, *9*, 290−294.
(58) Li, Y.; Zhao, T.; Wang, C.; Lin, Z.; Huang, G.; Sumer, B. D.; Gao, J. Molecular Basis of Cooperativity in pH-Triggered Supramolecular Self-Assembly. *Nat. Commun.* **2016**, *7*, 13214.
(59) Adolph, E. J.; Nelson, C. E.; Werfel, T. A.; Guo, R.; Davidson, J. M.; Guelcher, S. A.; Duvall, C. L. Enhanced Performance of Plasmid DNA Polyplexes Stabilized by a Combination of Core Hydrophobicity and Surface PEGylation. *J. Mater. Chem. B* **2014**, *2*, 8154−8164.
(60) Jackson, M. A.; Bedingfield, S. K.; Yu, F.; Stokan, M. E.; Miles, R. E.; Curvino, E. J.; Hoogenboezem, E. N.; Bonami, R. H.; Patel, S. S.; Kendall, P. L.; Giorgio, T. D.; Duvall, C. L. Dual Carrier-Cargo Hydrophobization and Charge Ratio Optimization Improve the Systemic Circulation and Safety of Zwitterionic Nano-Polyplexes. *Biomaterials* **2019**, *192*, 245−259.
(61) Wu, D.; Pusuluri, A.; Vogus, D.; Krishnan, V.; Shields, C. W.; Kim, J.; Razmi, A.; Mitragotri, S. Design Principles of Drug Combinations for Chemotherapy. *J. Controlled Release* **2020**, *323*, 36−46.
(62) Tan, Z.; Jiang, Y.; Ganewatta, M. S.; Kumar, R.; Keith, A.; Twaroski, K.; Pengo, T.; Tolar, J.; Lodge, T. P.; Reineke, T. M. Block Polymer Micelles Enable CRISPR/Cas9 Ribonucleoprotein Delivery: Physicochemical Properties Affect Packaging Mechanisms and Gene Editing Efficiency. *Macromolecules* **2019**, *52*, 8197−8206.
(63) Dosta, P.; Segovia, N.; Cascante, A.; Ramos, V.; Borrós, S. Surface Charge Tunability as a Powerful Strategy to Control Electrostatic Interaction for High Efficiency Silencing, Using Tailored Oligopeptide-Modified Poly(β-Amino Ester)s (PBAEs). *Acta Biomater.* **2015**, *20*, 82−93.
(64) Dunn, A. W.; Kalinichenko, V. V.; Shi, D. Highly Efficient *in Vivo* Targeting of the Pulmonary Endothelium Using Novel Modifications of Polyethylenimine: An Importance of Charge. *Adv. Healthcare Mater.* **2018**, *7*, 1800876.
(65) Fröhlich, E. The Role of Surface Charge in Cellular Uptake and Cytotoxicity of Medical Nanoparticles. *Int. J. Nanomed.* **2012**, *7*, 5577−5591.
(66) Staedtler, A. M.; Hellmund, M.; Sheikhi Mehrabadi, F.; Thota, B. N.; Zollner, T. M.; Koch, M.; Haag, R.; Schmidt, N. Optimized Effective Charge Density and Size of Polyglycerol Amines Leads to Strong Knockdown Efficacy *in Vivo*. *J. Mater. Chem. B* **2015**, *3*, 8993−9000.
(67) Ghosh, P. S.; Kim, C. K.; Han, G.; Forbes, N. S.; Rotello, V. M. Efficient Gene Delivery Vectors by Tuning the Surface Charge Density of Amino Acid-Functionalized Gold Nanoparticles. *ACS Nano* **2008**, *2*, 2213−2218.


https://dx.doi.org/10.1021/acsnano.0c08549
*ACS Nano* 2020, 14, 17626−17639